

Mott and generalized Wigner crystal states in WSe₂/WS₂ moiré superlattices

<https://doi.org/10.1038/s41586-020-2092-4>

Received: 19 August 2019

Accepted: 21 January 2020

Published online: 18 March 2020

 Check for updates

Emma C. Regan^{1,2,3,12}, Danqing Wang^{1,2,3,12}, Chenhao Jin^{14,12}, M. Iqbal Bakti Utama^{1,3,5}, Beini Gao¹⁶, Xin Wei¹⁷, Sihan Zhao¹, Wenyu Zhao¹, Zuocheng Zhang¹, Kentaro Yumigeta⁸, Mark Blei⁹, Johan D. Carlström¹⁹, Kenji Watanabe¹⁰, Takashi Taniguchi¹⁰, Sefaattin Tongay⁸, Michael Crommie^{1,3,11}, Alex Zettl^{1,3,11} & Feng Wang^{1,3,11}✉

Moiré superlattices can be used to engineer strongly correlated electronic states in two-dimensional van der Waals heterostructures, as recently demonstrated in the correlated insulating and superconducting states observed in magic-angle twisted-bilayer graphene and ABC trilayer graphene/boron nitride moiré superlattices^{1–4}. Transition metal dichalcogenide moiré heterostructures provide another model system for the study of correlated quantum phenomena⁵ because of their strong light–matter interactions and large spin–orbit coupling. However, experimental observation of correlated insulating states in this system is challenging with traditional transport techniques. Here we report the optical detection of strongly correlated phases in semiconducting WSe₂/WS₂ moiré superlattices. We use a sensitive optical detection technique and reveal a Mott insulator state at one hole per superlattice site and surprising insulating phases at 1/3 and 2/3 filling of the superlattice, which we assign to generalized Wigner crystallization on the underlying lattice^{6–11}. Furthermore, the spin–valley optical selection rules^{12–14} of transition metal dichalcogenide heterostructures allow us to optically create and investigate low-energy excited spin states in the Mott insulator. We measure a very long spin relaxation lifetime of many microseconds in the Mott insulating state, orders of magnitude longer than that of charge excitations. Our studies highlight the value of using moiré superlattices beyond graphene to explore correlated physics.

Moiré superlattices offer a general and powerful platform for engineering correlated electronic states in van der Waals heterostructures. We consider a simple but highly informative toy model: a two-dimensional electron gas in a periodic potential of periodicity L . The periodic potential leads to the formation of a set of minibands in the electron band structure. The electron–electron interaction U and the electronic bandwidth W of the lowest electronic miniband can be estimated as $U \approx e^2/(4\pi\varepsilon L)$ and $W \approx \frac{\hbar^2 k^2}{2m_e} \approx \frac{\hbar^2 \pi^2}{2m_e L^2}$, respectively, and the ratio U/W scales linearly with $m_e^* L$. Here ε is the effective dielectric constant, m_e^* is the electron effective mass, k is the wavevector, \hbar is the reduced Planck constant and e is the electron charge. Strong correlation (with $U/W > 1$) can be readily achieved with sufficiently large $m_e^* L$, for example, with a moiré superlattice ($L \approx 10$ nm) and an effective mass $m_e^* > 0.1m_0$ for $\varepsilon \approx 4\varepsilon_0$ (ε_0 , vacuum permittivity; m_0 , free electron mass). If the periodic moiré potential is very strong, the electron bandwidth W is additionally suppressed, further enhancing the correlation effects. The design criteria of large $m_e^* L$ can be satisfied in many moiré heterostructures. One such instance is the ABC trilayer graphene/boron nitride moiré

superlattice, which has tunable Mott insulator, superconductor and correlated Chern insulator states^{3,4,15}. Transition metal dichalcogenide (TMD) heterostructures represent another intriguing platform. The large effective mass ($m_e^* \approx 0.5m_0$) of TMDs^{16,17} can lead to many-body phenomena even in monolayer TMDs^{18,19}, and creates particularly strong correlation effects in moiré superlattices. Further, their strong light–matter interactions^{20,21} can enable optical detection and manipulation of the correlated quantum states of matter.

Here we report the observation of the Mott insulator state and generalized Wigner crystallization on an underlying lattice in semiconducting WSe₂/WS₂ moiré superlattices. By taking advantage of the strong light–matter interactions of TMDs, we optically detect both the quantum capacitance and electrical resistance of the moiré heterostructure while avoiding complications from very large contact resistances. A prominent example of a strongly correlated electronic system is the Mott insulator at one hole per superlattice site ($n = n_0$, where n is the hole concentration and n_0 corresponds to one hole per superlattice site)^{22,23}, as illustrated in Fig. 1a. We show that the Mott insulating state exists in WSe₂/WS₂ moiré superlattices at

¹Department of Physics, University of California at Berkeley, Berkeley, CA, USA. ²Graduate Group in Applied Science and Technology, University of California at Berkeley, Berkeley, CA, USA.

³Material Science Division, Lawrence Berkeley National Laboratory, Berkeley, CA, USA. ⁴Kavli Institute at Cornell for Nanoscale Science, Ithaca, NY, USA. ⁵Department of Materials Science and Engineering, University of California at Berkeley, Berkeley, CA, USA. ⁶Department of Physics, Huazhong University of Science and Technology, Wuhan, China. ⁷School of Physics, University of the Chinese Academy of Sciences, Beijing, China. ⁸School for Engineering of Matter, Transport and Energy, Arizona State University, Tempe, AZ, USA. ⁹Department of Physics, Lund University, Lund, Sweden. ¹⁰National Institute for Materials Science, Tsukuba, Japan. ¹¹Kavli Energy NanoSciences Institute at University of California Berkeley and Lawrence Berkeley National Laboratory, Berkeley, CA, USA. ¹²These authors contributed equally: Emma C. Regan, Danqing Wang, Chenhao Jin. [✉]e-mail: fengwang76@berkeley.edu

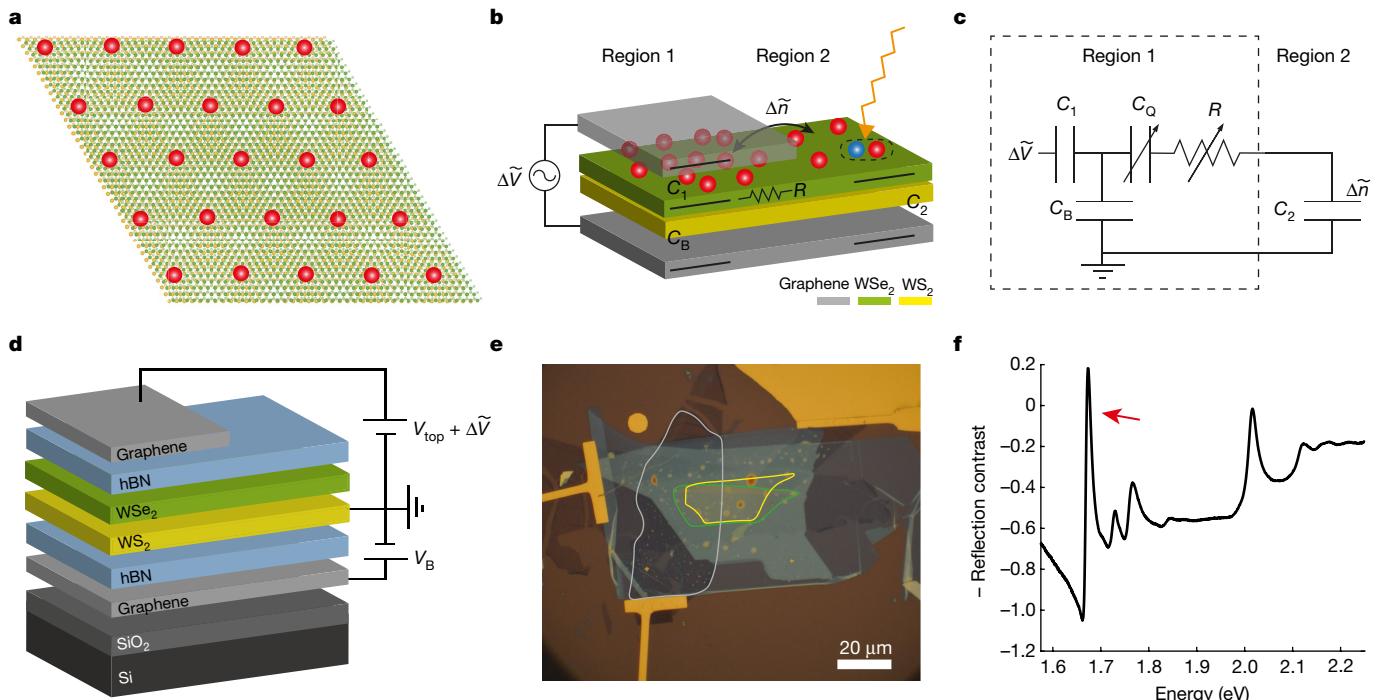


Fig. 1 | Optically detected resistance and capacitance technique in a WSe₂/WS₂ superlattice. **a**, Illustration of a Mott insulator state in a WSe₂/WS₂ moiré superlattice (green and orange layers) with one hole (red circles) per superlattice unit cell. **b, c**, Schematic of a device used for an ODRC measurement in a WSe₂/WS₂ heterostructure (**b**), which includes a local top gate and a global back gate. A small a.c. bias ($\Delta\tilde{V}$) leads to charge redistribution between region 1 and region 2 ($\Delta\tilde{n}$), which is detected via the change in the optical reflectivity of the WSe₂ exciton in region 2. This a.c. measurement can be modelled as an effective RC circuit (**c**). The elements of the circuit are shown schematically in **b**. C_1 , C_B and C_2 are the geometric capacitances in the system,

and R and C_Q are the doping-dependent resistance and quantum capacitance, respectively, of region 1 that we measure. **d, e**, Side-view illustration (**d**) and optical microscope image (**e**) of a heterostructure with near-zero twist angle (device D1). The graphite top gate, WS₂ and WSe₂ flakes are outlined in grey, yellow and green, respectively. **f**, Optical absorption spectrum of the heterostructure, showing splitting of the WSe₂ A exciton into three prominent peaks, which is characteristic of intralayer moiré excitons in an aligned heterostructure. The ODRC measurements use a laser probe in resonance with the lowest-energy exciton peak (red arrow).

temperatures of up to 45 K and has an estimated Mott–Hubbard gap of about 10 meV, an order of magnitude larger than that in graphene moiré systems. Surprisingly, we also observe additional insulating states from generalized Wigner crystallization at fractional fillings of $n = 1/3n_0$ and $n = 2/3n_0$. The emergence of these generalized Wigner crystal states necessitates an extended Hubbard model with not only on-site (short-range) but also inter-site (long-range) interactions^{7,8}. In addition, the strong light–matter interaction and unique spin–valley selection rules of TMD moiré heterostructures allow us to optically create and detect different elementary excitations associated with their strongly correlated ground states. We use circularly polarized light to generate a low-energy pure-spin excitation, and we demonstrate an increased spin lifetime at the Mott insulating state.

We investigate correlated states in a TMD heterostructure using the novel optically detected resistance and capacitance (ODRC) technique. The large semiconductor bandgap in TMDs leads to the formation of Schottky barriers at metal–TMD junctions and correspondingly large contact resistance. This large contact resistance often hampers direct electrical-transport measurements in TMD heterostructures, particularly for low carrier doping and at low temperatures²⁴. Our optical detection scheme avoids this difficulty. For the ODRC measurements, we design a special device configuration with two regions (Fig. 1b): one half of the device has a local graphite top gate (region 1), and the other half does not (region 2). We vary the d.c. voltage on the local top gate (V_{top}) to continuously control the carrier doping in region 1, where the charge injection occurs with a time constant of about 1 s. We then add an a.c. excitation voltage

($\Delta\tilde{V}$) to the local top gate. For excitation frequencies higher than 10 Hz, the electrical contact is effectively frozen and the TMD heterostructure is floated electrically (see Methods). In this case, the a.c. excitation voltage leads only to charge redistribution between region 1 and region 2, with no total charge change, and the charge redistribution dynamics depends on the quantum capacitance and resistance in the moiré system. We detect the resulting change of carrier concentration in region 2 ($\Delta\tilde{n}$) optically, through the induced change in optical contrast ΔOC at the intralayer exciton resonance (see Methods, Extended Data Fig. 1). The global graphite back gate is used to set the d.c. doping level of region 2 to optimize the exciton optical response to doping changes.

The a.c. electrical transport in the TMD heterostructure can be modelled by an effective RC circuit, shown in Fig. 1c. Here C_1 and C_B are the geometric capacitances between the TMD and the top and bottom gates in region 1, respectively, and C_2 is the TMD–bottom gate capacitance in region 2. These geometric capacitances C_i ($i = 1, 2, B$) are set by $C_i = \epsilon_0 \epsilon_r A_i / d_i$, where ϵ_r is the dielectric constant of the gate dielectric, and A_i and d_i denote the relevant capacitor area and separation, respectively. The parameters to be measured are C_Q and R , which correspond to the doping-dependent quantum capacitance and resistance of the moiré superlattice in region 1, respectively. The induced optical contrast change ΔOC in region 2 upon an a.c. capacitive excitation $\Delta\tilde{V}$ in region 1 can be obtained from the effective circuit model (see Supplementary Information) as

$$\Delta OC = \alpha \Delta\tilde{n} = \frac{\alpha}{A_2 e} \Delta\tilde{V} \frac{C_1}{C_1 + C_B} \frac{1}{\frac{1}{C_{eff}} + i\omega R} \quad (1)$$

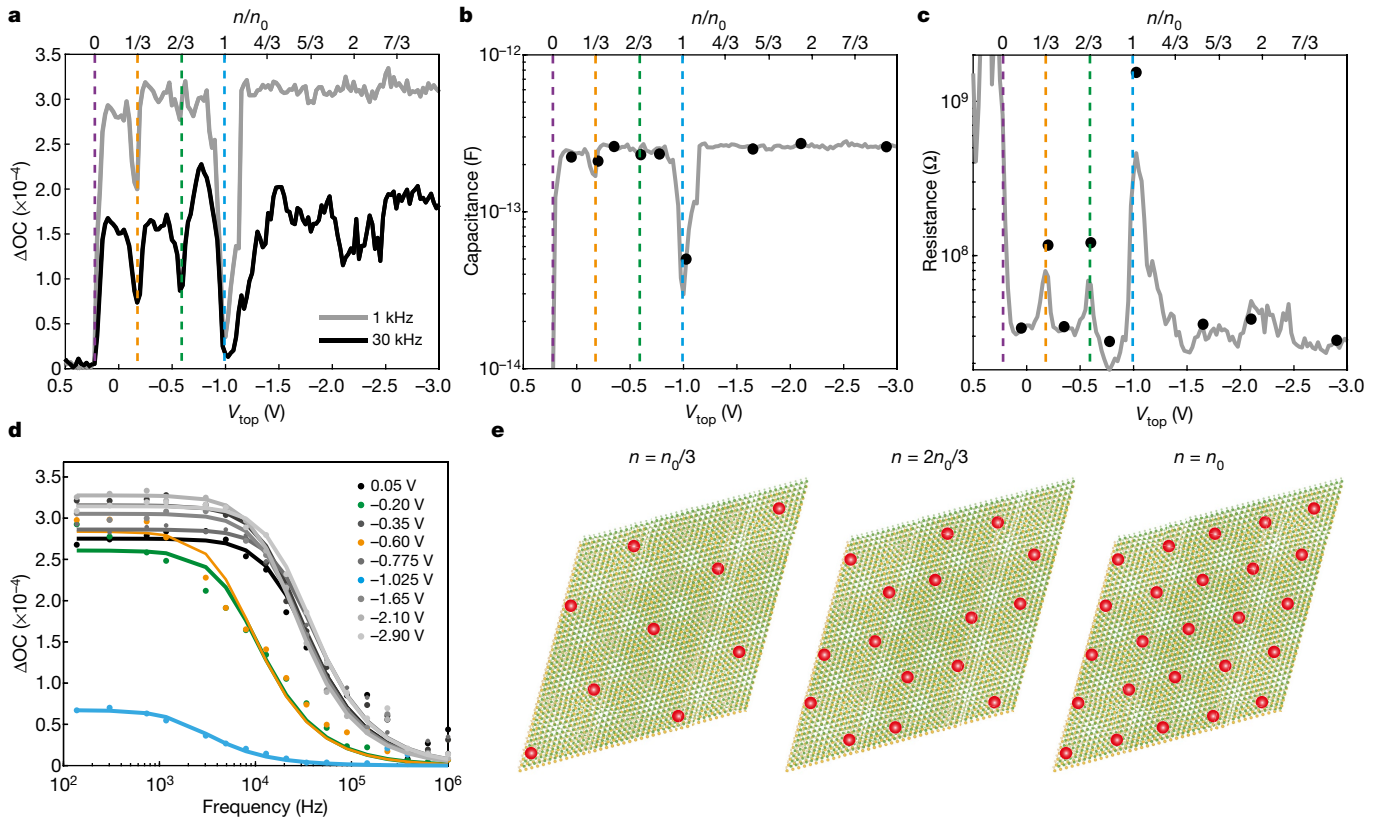


Fig. 2 | Doping-dependent resistance and capacitance probed by ODRC.

a, ODRC signal at 1 kHz (grey) and 30 kHz (black) from charge-neutral to moderate hole doping. Strong gap-like features are observed at hole doping levels of $n = n_0/3$ (orange dashed line), $n = 2n_0/3$ (green dashed line) and $n = n_0$ (blue dashed line). The purple dashed line corresponds to $n = 0$. **b–d**, Capacitance C_{eff} (**b**) and resistance (**c**) of region 1. Grey curves are extracted from the data in **a**, and black dots are extracted from the frequency-

dependent ODRC signal (**d**) at representative doping levels. In **d**, the dots are the frequency-dependent ODRC signal at the indicated values of V_{top} and the lines are the corresponding fits with the RC circuit model. The decreased capacitance and increased resistance indicate emerging insulating states at $n = n_0/3$, $n = 2n_0/3$ and $n = n_0$. All measurements are done at 3 K. **e**, Illustrations of generalized Wigner crystal ($n = n_0/3$, $n = 2n_0/3$) and Mott insulator states ($n = n_0$) in a WSe₂/WS₂ moiré superlattice.

with

$$\frac{1}{C_{\text{eff}}} = \frac{1}{C_1 + C_B} + \frac{1}{C_2} + \frac{1}{C_Q}$$

Here ω is the excitation frequency and $\alpha = \Delta\text{OC}/\Delta\tilde{\omega}$ is the optical detection responsivity in region 2, which is constant for the fixed bottom gate voltage used in our study. The frequency-dependent optical signal $\Delta\text{OC}(\omega)$ allows us to extract the values of both C_Q and R : at low excitation frequencies the resistance is negligible, so the optical signal probes the quantum capacitance C_Q , which is proportional to the density of states of the moiré heterostructure. At high modulation frequencies, both C_Q and R contribute to the optical signal.

We focus our study on WSe₂/WS₂ heterostructures with near-zero twist angles that have a moiré superlattice with a period of about 8 nm owing to the -4% lattice mismatch between the WS₂ and WSe₂ monolayers. Figure 1d shows a schematic of device D1: few-layer graphene is used for the gates and contact to the TMD layers, and hexagonal boron nitride (hBN) is used at the top and bottom gate dielectrics ($\epsilon_r = 4.2$; see Methods and ref.²⁵ for fabrication details). Figure 1e shows an optical microscopy image of the final device, with contours highlighting the WS₂ and WSe₂ layers and the local graphite top gate. To verify the presence of the moiré superlattice, we examine the optical absorption spectrum of the heterostructure (Fig. 1f). The spectrum shows clear splitting of the WSe₂A exciton, which is a signature of the moiré superlattice in the heterostructure²⁵.

Figure 2a shows the ODRC signals as a function of the hole doping of the WSe₂/WS₂ moiré superlattice in region 1. We use an a.c. excitation

voltage with the peak-to-peak amplitude of 10 mV at 1 kHz and 30 kHz. When region 1 is charge-neutral ($V_{\text{top}} > 0.2$ V), the ΔOC signal is small because no carriers are available to redistribute in the bandgap of WSe₂. When region 1 is hole-doped ($V_{\text{top}} < 0.2$ V), charge redistribution occurs, leading to a large increase in the signal. Interestingly, we observe a strong gap-like feature at -1 V (blue dashed line in Fig. 2a). From a capacitance model, we estimate the corresponding hole concentration to be $1.86 \times 10^{12} \text{ cm}^{-2}$, which matches well with a density of one hole per moiré unit cell ($n_0 = 1.88 \times 10^{12} \text{ cm}^{-2}$; see Methods). We also observe two sharp dips at -0.2 V and -0.6 V (orange and green dashed lines in Fig. 2a), which correspond to hole concentrations of $n = n_0/3$ and $n = 2n_0/3$, respectively. Additionally, a broad, weaker feature is observed at -2.25 V, which corresponds to $n = 2n_0$. These features become stronger at the higher excitation frequency of 30 kHz. ODRC signals for additional aligned heterostructures are shown in Extended Data Fig. 5.

We extract numerical values for the doping-dependent C_{eff} and R of the moiré heterostructure based on the effective a.c. circuit model and equation (1). We plot C_{eff} and R as a function of carrier doping in Fig. 2b, c (grey lines). An optical responsivity of $\alpha = 1.4 \times 10^{-12} \text{ cm}^2$ is chosen so that $\frac{1}{C_{\text{eff}}} = \frac{1}{C_1 + C_B} + \frac{1}{C_2}$ at high doping, where the quantum capacitance is much larger than the geometric capacitances and has negligible contribution. At $n = n_0$, $n = n_0/3$ and $n = 2n_0/3$, C_{eff} decreases, whereas the geometric capacitances remain unchanged (Fig. 2b). This decrease in C_{eff} is due to the much smaller quantum capacitance C_Q , which results from the greatly reduced density of states at these fillings. At the same time, the electrical resistance shows marked increases at $n = n_0$, $n = n_0/3$ and $n = 2n_0/3$ (Fig. 2c). The simultaneous reduction of the density of

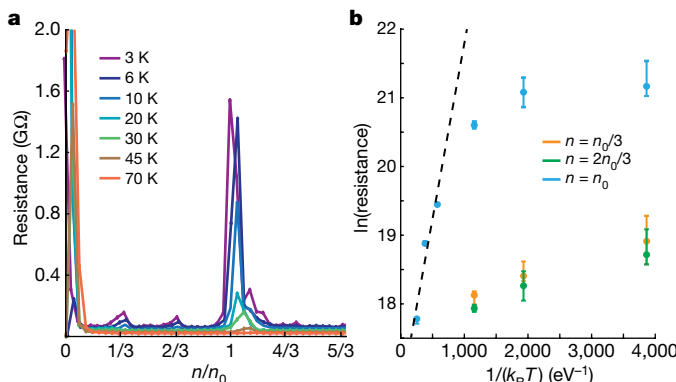


Fig. 3 | Temperature dependence of Mott and generalized Wigner crystal states. **a**, Resistance derived from ODRC measurements performed at temperatures between 3 K and 70 K. The Mott insulator state at $n = n_0$ is observable up to 45 K, and the generalized Wigner crystal states at $n = n_0/3$ and $n = 2n_0/3$ persist until 10 K. **b**, Plot of $\ln(\text{resistance})$ versus $1/k_B T$ for Mott (blue) and generalized Wigner crystal states (orange and green). Error bars correspond to the estimated experimental uncertainty in the extracted resistance values. The estimated thermal-activation gap for the Mott state is about 10 meV, which is found by fitting the data in **b** with a thermal-activation function (black dashed line).

states and large increase of the resistance indicate the emergence of insulating states at these fillings.

To test our effective circuit model quantitatively, we measure the frequency dependence of the ODRC signal at several representative hole-doping densities. Figure 2d displays the experimental results (symbols). We observe a clear signal fall-off with increasing frequency, and the data can be reproduced by the circuit model predictions (solid lines). The effective capacitance and resistance at these fillings extracted from the frequency dependence of the ODRC signal (black dots in Fig. 2b, c) agree well with the values extracted directly from the data in Fig. 2a.

Our results show that the WSe₂/WS₂ moiré heterostructure hosts insulating states with reduced density of states and increased resistance at $n = n_0$, $n = n_0/3$ and $n = 2n_0/3$. These features are completely absent in large-twist-angle WSe₂/WS₂ heterostructures (see Methods, Extended Data Fig. 6) and only emerge in the moiré superlattices. The insulating state at $n = n_0$ is typically assigned to a Mott insulator^{22,23} but may also be considered to be an interaction-driven Wigner crystal state^{6–11} or a charge-transfer insulator²⁶ (Fig. 2e). This state corresponds to half-filling of the moiré miniband because the TMD heterostructure has a degeneracy of 2 from spin-valley locking¹³. Similar correlated insulating

states have also been observed at $n = n_0$ in twisted bilayer graphene and ABC trilayer graphene/boron nitride moiré superlattices^{1–4}.

On the other hand, the observation of insulating states at $n = n_0/3$ and $n = 2n_0/3$ is surprising. Insulating states at fractional filling of the lattice sites have not been observed in other moiré superlattice systems and cannot be described as a Mott insulator or by a Hubbard model with only on-site repulsive interactions. We hypothesize that these insulating states at $n = n_0/3$ and $n = 2n_0/3$ correspond to generalized Wigner crystallization^{6–11} of holes in the TMD moiré superlattice. Figure 2e illustrates the real-space configurations of the generalized Wigner crystal states, where holes try to avoid not only double occupation in one site, but also simultaneous occupation of adjacent sites. There are three degenerate Wigner crystallization configurations. The TMD moiré system spontaneously breaks the lattice translational symmetry owing to electron–electron interactions and condenses to one specific configuration with a $\sqrt{3} \times \sqrt{3}$ charge density wave pattern. The emergence of these generalized Wigner crystal states suggests that even the inter-site (long-range) interaction energy is larger than the moiré miniband bandwidth, confirming the very strong correlation in the TMD moiré heterostructure.

We perform ODRC measurements of the doping-dependent quantum capacitance and resistance of the TMD moiré superlattices at different temperatures. Figure 3a shows the extracted resistance for temperatures from 3 K to 70 K. The resistance peaks of the Mott insulator and generalized Wigner crystal states are observable up to temperatures of 45 K and 10 K, respectively. We estimate the Mott–Hubbard gap to be $\Delta \approx 10$ meV by fitting the resistance with a thermal-activation function, $\exp[-\Delta/(2k_B T)]$ (k_B , Boltzmann constant; T , temperature), for the Mott insulator state at $n = n_0$ (black dashed line in Fig. 3b). Owing to the limited range exhibiting thermal-activation behaviour, the estimated Mott gap has relatively large uncertainty. It is difficult to estimate the size of the insulating gaps of the generalized Wigner crystal states from the experimental data, but they are probably 5–10 times smaller than the Mott insulator gap according to the temperature at which the generalized Wigner crystal signatures disappear.

The strong electron correlation and light–matter interaction in the heterostructure provides unique opportunities to optically investigate excited states from the correlated phases, such as low-energy charge and spin excitations. Charge excitations in Mott insulator systems have been intensively studied, featuring ultrafast decay dynamics (typically a few picoseconds) from the holon–doublon recombination process^{27–29}. On the other hand, the dynamics of pure spin excitations are difficult to explore. Here we directly measure the doping-dependent decay of a pure spin excitation by taking advantage of the unique spin–valley selection rules in the TMD heterostructure^{12–14}. We use the pump–probe scheme described in refs.^{30,31} to generate and probe the spin excitation

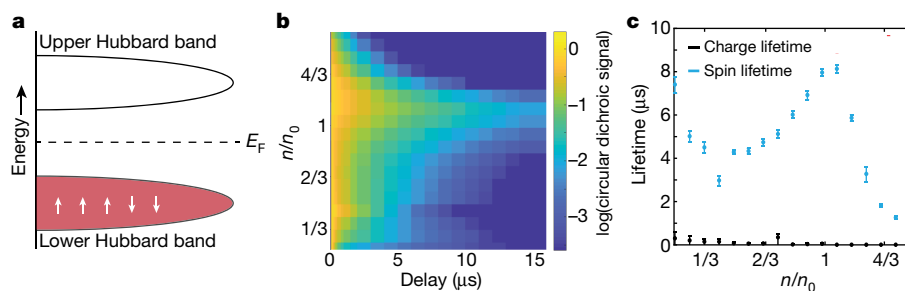


Fig. 4 | Optical investigation of low-energy spin excitation dynamics of a WSe₂/WS₂ Mott insulator. **a**, A circularly polarized pump pulse selectively excites K-valley excitons with spin-up electrons and holes in the moiré heterostructure. After a fast charge recombination process, an excess of spin-polarized holes remains in the lower Hubbard band. The evolution of this low-energy spin excitation can be measured by a second probe pulse through

pump-induced circular dichroic signals. **b**, Doping-dependent decay dynamics of the optically generated pure spin excitations. **c**, Spin (blue) and charge (black) lifetimes as a function of hole doping. The spin relaxation slows down markedly near $n = n_0$, with a lifetime as long as 8 μs. By contrast, the total charge population decays quickly for all doping levels.

in the moiré heterostructure at 20 K. Specifically, a circularly polarized pump excitation is employed to selectively excite K-valley excitons composed of spin-up holes and electrons. The relaxation of the spin-polarized electrons and holes within about 100 ns results in a residual spin polarization in the lower Hubbard band of the Mott insulator, as illustrated in Fig. 4a. We probe the evolution of the residual spin polarization through the pump-induced circular dichroic signal and the charge population through the pump-induced change in the total absorption of the probe beam. Figure 4b shows the time evolution of the spin population at different hole densities. The doping-dependent spin lifetime, represented by blue symbols in Fig. 4c, shows a prominent increase at the Mott insulator state ($n = n_0$) and reaches more than 8 μ s. By contrast, the lifetime of charge excitations (black symbols) is orders of magnitude shorter. The long-lived spin excitations from the Mott insulator state can provide important information about its spin configuration. It has been proposed that the Mott insulator state in the WSe₂/WS₂ moiré superlattice can host intriguing spin states, such as the quantum spin liquid^{32,33}. However, further theoretical studies will be required to understand the experimentally observed spin dynamics in the Mott insulating state, which is beyond the scope of this paper.

Our results demonstrate that TMD moiré heterostructures can host novel quantum correlated phases and offer an attractive platform for probing excited-state and non-equilibrium dynamics of the correlated phases owing to a unique combination of highly correlated electrons, strong light-matter interactions and a large spin-orbit effect in the system.

Online content

Any methods, additional references, Nature Research reporting summaries, source data, extended data, supplementary information, acknowledgements, peer review information; details of author contributions and competing interests; and statements of data and code availability are available at <https://doi.org/10.1038/s41586-020-2092-4>.

1. Cao, Y. et al. Correlated insulator behaviour at half-filling in magic-angle graphene superlattices. *Nature* **556**, 80–84 (2018).
2. Cao, Y. et al. Unconventional superconductivity in magic-angle graphene superlattices. *Nature* **556**, 43–50 (2018).
3. Chen, G. et al. Evidence of a gate-tunable Mott insulator in a trilayer graphene moiré superlattice. *Nat. Phys.* **15**, 237–241 (2019).
4. Chen, G. et al. Signatures of tunable superconductivity in a trilayer graphene moiré superlattice. *Nature* **572**, 215–219 (2019).
5. Wu, F., Lovorn, T., Tutuc, E. & MacDonald, A. H. Hubbard model physics in transition metal dichalcogenide moiré bands. *Phys. Rev. Lett.* **121**, 026402 (2018).
6. Wigner, E. On the interaction of electrons in metals. *Phys. Rev.* **46**, 1002–1011 (1934).
7. Hubbard, J. Generalized Wigner lattices in one dimension and some applications to tetracyanoquinodimethane (TCNQ) salts. *Phys. Rev. B* **17**, 494–505 (1978).
8. Wu, C., Bergman, D., Balents, L. & Das Sarma, S. Flat bands and Wigner crystallization in the honeycomb optical lattice. *Phys. Rev. Lett.* **99**, 070401 (2007).
9. Hiraki, K. & Kanoda, K. Wigner crystal type of charge ordering in an organic conductor with a quarter-filled band: (D1-DCNQI)_xAg. *Phys. Rev. Lett.* **80**, 4737–4740 (1998).
10. Padhi, B., Setty, C. & Phillips, P. W. Doped twisted bilayer graphene near magic angles: proximity to Wigner crystallization, not Mott insulation. *Nano Lett.* **18**, 6175–6180 (2018).
11. Padhi, B. & Phillips, P. W. Pressure-induced metal-insulator transition in twisted bilayer graphene. *Phys. Rev. B* **99**, 051401 (2019).
12. Mak, K. F., He, K., Shan, J. & Heinz, T. F. Control of valley polarization in monolayer MoS₂ by optical helicity. *Nat. Nanotechnol.* **7**, 494–498 (2012).
13. Xiao, D., Liu, G.-B., Feng, W., Xu, X. & Yao, W. Coupled spin and valley physics in monolayers of MoS₂ and other group-VI dichalcogenides. *Phys. Rev. Lett.* **108**, 196802 (2012).
14. Cao, T. et al. Valley-selective circular dichroism of monolayer molybdenum disulphide. *Nat. Commun.* **3**, 887 (2012).
15. Chen, G. et al. Tunable correlated Chern insulator and ferromagnetism in trilayer graphene/boron nitride moiré superlattice. Preprint at <https://arxiv.org/abs/1905.06535> (2019).
16. Kadantsev, E. S. & Hawrylak, P. Electronic structure of a single MoS₂ monolayer. *Solid State Commun.* **152**, 909–913 (2012).
17. Fallahazad, B. et al. Shubnikov-de Haas oscillations of high-mobility holes in monolayer and bilayer WSe₂: Landau level degeneracy, effective mass, and negative compressibility. *Phys. Rev. Lett.* **116**, 086601 (2016).
18. Roch, J. G. et al. Spin-polarized electrons in monolayer MoS₂. *Nat. Nanotechnol.* **14**, 432–436 (2019).
19. Back, P. et al. Giant paramagnetism-induced valley polarization of electrons in charge-tunable monolayer MoSe₂. *Phys. Rev. Lett.* **118**, 237404 (2017).
20. Splendiani, A. et al. Emerging photoluminescence in monolayer MoS₂. *Nano Lett.* **10**, 1271–1275 (2010).
21. Mak, K. F., Lee, C., Hone, J., Shan, J. & Heinz, T. F. Atomically thin MoS₂: a new direct-gap semiconductor. *Phys. Rev. Lett.* **105**, 136805 (2010).
22. Mott, N. F. The basis of the electron theory of metals, with special reference to the transition metals. *Proc. Phys. Soc. A* **62**, 416–422 (1949).
23. Imada, M., Fujimori, A. & Tokura, Y. Metal-insulator transitions. *Rev. Mod. Phys.* **70**, 1039–1263 (1998).
24. Allain, A., Kang, J., Banerjee, K. & Kis, A. Electrical contacts to two-dimensional semiconductors. *Nat. Mater.* **14**, 1195–1205 (2015).
25. Jin, C. et al. Observation of moiré excitons in WSe₂/WS₂ heterostructure superlattices. *Nature* **567**, 76–80 (2019); correction 569, E7 (2019).
26. Zhang, Y., Yuan, N. F. Q. & Fu, L. Moiré quantum chemistry: charge transfer in transition metal dichalcogenide superlattices. Preprint at <https://arxiv.org/abs/1910.14061> (2019).
27. Lenaričić, Z. & Prelović, P. Ultrafast charge recombination in a photoexcited Mott-Hubbard insulator. *Phys. Rev. Lett.* **111**, 016401 (2013).
28. Okamoto, H. et al. Photoinduced transition from Mott insulator to metal in the undoped cuprates. *Phys. Rev. B* **83**, 125102 (2011).
29. Giannetti, C. et al. Ultrafast optical spectroscopy of strongly correlated materials and high-temperature superconductors: a non-equilibrium approach. *Adv. Phys.* **65**, 58–238 (2016).
30. Kim, J. et al. Observation of ultralong valley lifetime in WSe₂/MoS₂ heterostructures. *Sci. Adv.* **3**, e1700518 (2017).
31. Jin, C. et al. Imaging of pure spin-valley diffusion current in WS₂/WSe₂ heterostructures. *Science* **360**, 893–896 (2018).
32. Law, K. T. & Lee, P. A. 1T-TaS₂ as a quantum spin liquid. *Proc. Natl Acad. Sci. USA* **114**, 6996–7000 (2017).
33. Grover, T., Trivedi, N., Senthil, T. & Lee, P. A. Weak Mott insulators on the triangular lattice: Possibility of a gapless nematic quantum spin liquid. *Phys. Rev. B* **81**, 245121 (2010).

Publisher's note Springer Nature remains neutral with regard to jurisdictional claims in published maps and institutional affiliations.

© The Author(s), under exclusive licence to Springer Nature Limited 2020

Article

Methods

ODRC measurements

A function generator (Rigol 1022Z) is used to generate the top-gate voltage, which consists of a d.c. offset, V_{top} , and a small a.c. modulation, $\Delta \tilde{V}$. A voltage source (Keithley 2400) is used for the back-gate voltage. A laser diode with centre energy of 1.66 eV serves as the probe light. The diode energy is fine-tuned using a thermoelectric cooler so that the probe energy is resonant with the lowest-energy WSe₂ A exciton absorption peak in region 2. The reflected probe light is collected with an avalanche photodiode (Thorlabs APD 410A) and then analysed using a lock-in amplifier that is locked to the function generator output.

WSe₂ A exciton absorption in region 2

The lowest-energy WSe₂ A exciton in region 2 is used to measure the electrical properties of region 1 as the local top gate is tuned. To be a reliable probe, the exciton in region 2 must respond only to charge redistribution due to the modulation voltage $\Delta \tilde{V}$, but not to the d.c. bias applied to the local top gate, V_{top} . We measure the optical spectrum of the lowest-energy WSe₂ A exciton (1.6–1.74 eV) while sweeping V_{top} from 0.5 V to –3.5 V (Extended Data Fig. 1a). We record the spectrum 15 s after changing V_{top} to ensure that the contact injects charge. We observe almost no change in the spectrum. Therefore, the static local top gate does not influence the hole concentration in region 2, and it remains a stable probe for all V_{top} values used.

We measure the absorption spectrum as a function of the carrier density in region 2 by varying the global back-gate voltage. Extended Data Fig. 1b shows the absorption spectra when the back-gate voltage is tuned in a small range around –1 V. For the ODRC measurement, the modulation voltage $\Delta \tilde{V}$ is typically set to 10–25 mV, so the redistributed charges correspond to a small back-gate voltage change of <25 mV. Within this range, the exciton resonance (1.673 eV) shows monotonic and linear change with carrier concentration. Therefore, the optical detection responsivity α is a constant for our choice of back-gate voltage.

We estimate an optical detection responsivity $\alpha = 1.4 \times 10^{-12} \text{ cm}^2$. The noise of the ODRC signal is $\sim 2 \times 10^{-6}$ in our lock-in measurement for 3 s averaging time. This allows us to detect a carrier density change in region 2 as small as 10^6 cm^{-2} with optical detection.

Low-frequency behaviour of ODRC signal

Extended Data Figure 2 shows the frequency-dependent ODRC signal at $V_{\text{top}} = -1.6$ V (that is, away from any features) for modulation frequencies between 0.05 Hz and 137 Hz. The carrier injection through the graphite contact has a characteristic time constant of ~1 s. At the lowest modulation frequency (0.05 Hz), the graphite contact can efficiently inject charge in response to $\Delta \tilde{V}$. As a result, the carrier density in region 2 remains constant and the overall ODRC signal is negligible. At 1 Hz, the ODRC signal is partially reduced compared with higher-frequency responses because the contact can inject some charge in response to $\Delta \tilde{V}$. For frequencies higher than ~10 Hz, the contact becomes frozen. As a result, the heterostructure is effectively floated and the ODRC signal reaches its typical low-frequency value. We also note that the ODRC signal is linear with $\Delta \tilde{V}$.

Heterostructure preparation for optical measurements

We use a dry-transfer method with a polyethylene terephthalate (PET) stamp to fabricate the WSe₂/WS₂ heterostructures³⁴. Monolayer WSe₂, monolayer WS₂, few-layer graphene and thin hBN flakes are first exfoliated onto Si substrates with a 90-nm-thick SiO₂ layer. For aligned heterostructures, we use polarization-dependent second-harmonic generation (SHG) to determine the crystal axes of WS₂ and WSe₂^{35,36}. We then use a PET stamp to pick up the few-layer graphene top gate, top hBN flake, the WS₂ monolayer, the WSe₂ monolayer, the few-layer-graphene contact, the bottom hBN flake and the few-layer graphene

back gate in sequence. Between picking up WSe₂ and WSe₂, we adjust the angle of the PET stamp to ensure a near-zero twist angle between the flakes. The PET stamp with the above heterostructure is then stamped onto a clean Si substrate with 90 nm SiO₂. The PET and samples are heated to 60 °C during the pick-up and to 130 °C for the stamping process. Finally, we dissolve the PET in dichloromethane overnight at room temperature. Contacts (~75 nm gold with a ~5-nm-thick chromium adhesion layer) to the few-layer graphene flakes are made using electron-beam lithography and electron-beam evaporation. Finally, we measure the polarization-dependent SHG on the monolayer TMDs in the heterostructure to determine the twist angle (see Extended Data Fig. 4).

Calibration of hBN dielectric constant

We directly calibrated the hBN dielectric constant against the known dielectric constant of SiO₂ using a dual-gate TMD device with a graphite top gate (with hBN as the gate dielectric) and a Si back gate (with SiO₂ as the gate dielectric). Specifically, we fabricated a dual-gated MoSe₂ device with a 45-nm-thick top hBN gate and a 290-nm-thick SiO₂/Si back gate. The hBN crystal is from the same batch that was used to fabricate our WSe₂/WS₂ moiré heterostructure devices. Extended Data Fig. 3a shows the MoSe₂ A exciton peak intensity as a function of the top- and back-gate voltages. Extended Data Fig. 3b shows the extracted charge-neutral points for each Si back gate, which correspond to the top graphite gate voltages that bring the system to zero net charge. The data show a linear behaviour and the slope indicates the relative gate efficiency. The hBN dielectric constant was then obtained using a parallel-plate capacitor model. The hBN thickness was determined by calibrated atomic force microscopy measurements, and the SiO₂ thickness was verified by the optical reflection spectrum. We obtain a hBN dielectric constant of 4.2 ± 0.4 using the SiO₂ dielectric constant of 3.9.

Determination of the relative twist angle between WSe₂ and WS₂ layers

The twist angle between the WSe₂ and WS₂ flakes in device D1 is $0.4^\circ \pm 0.3^\circ$, as determined via polarization-dependent SHG (Extended Data Fig. 4)^{25,35,36}. The SHG signal is four times larger on the heterostructure than on the monolayer regions, indicating that this device is closer to 0° than 60°.

Determination of moiré density n_0

The moiré density n_0 corresponds to one hole per moiré unit cell, and it is directly determined by the moiré periodicity through $n_0 = 1/[L_M^2 \sin(\pi/3)]$. Here $L_M = a/\sqrt{\delta^2 + \theta^2}$ is the moiré superlattice constant, $\delta = (a - a')/a \approx 4\%$ is the lattice mismatch between WSe₂ ($a = 0.328 \text{ nm}$) and WS₂ ($a' = 0.315 \text{ nm}$) and θ is the twist angle between the two layers. At θ smaller than ~1°, L_M is mainly determined by the intrinsic lattice constant mismatch between the two layers, so n_0 is not sensitive to a small uncertainty in θ . For device D1, we measured θ to be $0.4^\circ \pm 0.3^\circ$ using angle-dependent SHG. This corresponds to $n_0 = 1.88 \times 10^{12} \text{ cm}^{-2}$ with an experimental uncertainty of ~10%.

ODRC results from additional near-aligned heterostructures

We measured three near-aligned WSe₂/WS₂ moiré heterostructures (twist angle <1°). Extended Data Fig. 5a, b shows the ODRC signal of the other two devices, D2 and D3. The qualitative behaviour of the Mott insulator and generalized Wigner crystal states that are observed in D1 and described in the main text is reproducible in these devices. We observe a clear increase in the resistance and decrease in the ΔOC signal at the Mott states and the generalized Wigner crystal state at $n = 1/3n_0$. However, at $n = 2/3n_0$ the generalized Wigner crystal state is almost not observable. We do notice that devices D2 and D3 have much larger inhomogeneous broadening compared with device D1, as shown by the much broader width of the resistance peak. Presumably, the $n = 2/3n_0$

state is much more fragile than the Mott insulator and the $n = 1/3n_0$ state, and it is completely smeared out by the large inhomogeneous broadening in D2 and D3.

ODRC signal in a large-twist-angle WSe₂/WS₂ heterostructure

We measured the ODRC signal for a large-twist-angle WSe₂/WS₂ heterostructure, D4. In this device, the monolayer WSe₂ and WS₂ flakes are intentionally misaligned, and the absorption spectrum is characteristic of a large-twist-angle heterostructure. The signal from the misaligned heterostructure also shows a sharp increase when doped below the bandgap (red curve in Extended Data Fig. 6a), indicating that charge redistribution occurs. However, the signal is largely flat and does not show any clear dips corresponding to insulating states, in sharp contrast with the aligned case (blue curve). This observation is consistent with our conclusion that the insulating states in the aligned heterostructure are Mott and generalized Wigner states in the moiré superlattice, which is not present in a large-twist-angle heterostructure. Extended Data Fig. 6b presents the ODRC signal at several representative frequencies, which shows a characteristic RC circuit fall-off with increasing frequency. No additional feature is observed in the hole-doping region up to a frequency of 1 MHz, further confirming the absence of insulating states. The overall lower resistance in the misaligned device may be due to the different back-gate doping used in the two measurements.

Generation of optical pump–probe pulses with controlled time delay

Two electronic pulse generators (HP 8082A and HP 214B) were used to generate optical pump and probe pulses separately. Both pulse generators were triggered by the digital output of a data acquisition card, so the period and delay of the two triggering signals could be directly controlled with a computer. The output electronic pulses with ~20 ns pulse duration were then converted to optical pulses by two radiofrequency-coupled laser diode modules with energies of 1.80 eV (pump) and 1.66 eV (probe). The pump and probe beams were focused on the sample with beam-spot diameters of ~30 μm and ~5 μm,

respectively. Their polarizations were set using linear polarizers and a shared quarter-wave plate. The reflected probe light was collected by a photomultiplier tube. The pump–probe signal was analysed using a lock-in amplifier with modulation frequency of ~2.5 kHz.

Data availability

The data that support the findings of this study are available from the corresponding author upon reasonable request.

34. Wang, L. et al. One-dimensional electrical contact to a two-dimensional material. *Science* **342**, 614–617 (2013).
35. Kumar, N. et al. Second harmonic microscopy of monolayer MoS₂. *Phys. Rev. B* **87**, 161403 (2013).
36. Li, Y. et al. Probing symmetry properties of few-layer MoS₂ and h-BN by optical second-harmonic generation. *Nano Lett.* **13**, 3329–3333 (2013).

Acknowledgements We thank S. Li for discussions, S. Wang for help with device fabrication, and C. Stansbury and C. Wang for assistance with figure design. This work was supported primarily by the US Department of Energy, Office of Science, Office of Basic Energy Sciences, Materials Sciences and Engineering Division under contract number DE-AC02-05-CH1231 (van der Waals heterostructures programme, KCWF16). The device fabrication was also supported by the US Army Research Office under MURI award W911NF-17-1-0312. E.C.R. acknowledges support from the Department of Defense through the National Defense Science & Engineering Graduate Fellowship (NDSEG) Program. C.J. acknowledges support from a Kavli Postdoctoral Fellowship. S.T. acknowledges support from NSF DMR-1552220 and 1838443.

Author contributions F.W. conceived the research. E.C.R., D.W. and C.J. carried out optical measurements. D.W., E.C.R., C.J. and F.W. performed data analysis. E.C.R., D.W., B.G., X.W., M.I.B.U., S.Z., W.Z., Z.Z., J.D.C., M.C. and A.Z. contributed to the fabrication of van der Waals heterostructures. K.Y., M.B. and S.T. grew WSe₂ and WS₂ crystals. K.W. and T.T. grew hBN crystals. All authors discussed the results and wrote the manuscript.

Competing interests The authors declare no competing interests.

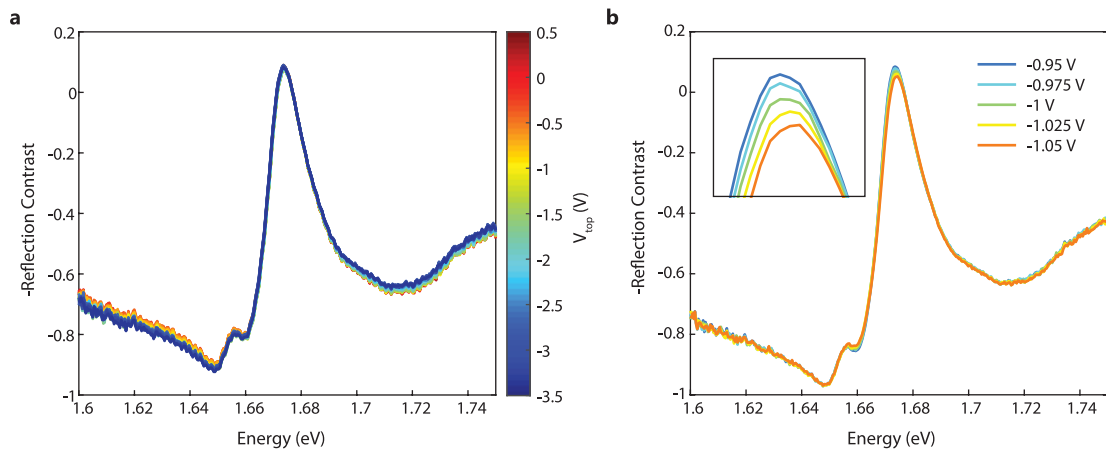
Additional information

Supplementary information is available for this paper at <https://doi.org/10.1038/s41586-020-2092-4>.

Correspondence and requests for materials should be addressed to F.W.

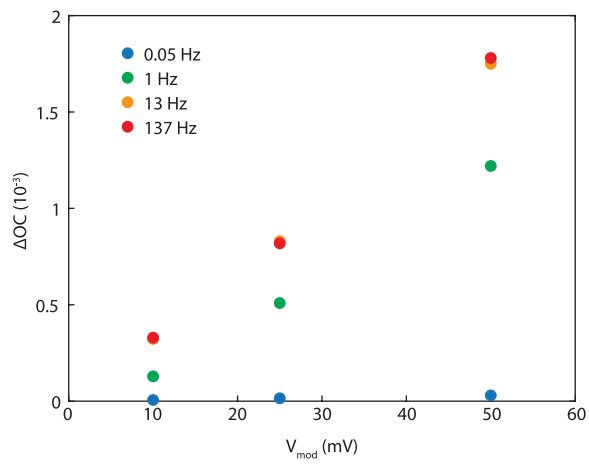
Peer review information *Nature* thanks Alexander Tartakovskii and the other, anonymous, reviewer(s) for their contribution to the peer review of this work.

Reprints and permissions information is available at <http://www.nature.com/reprints>.

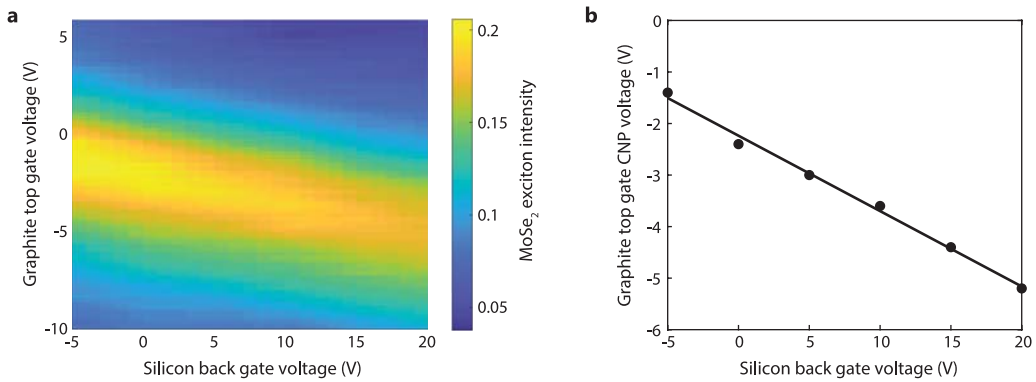


Extended Data Fig. 1 | WSe₂-A exciton gate behaviour. **a**, Reflection contrast spectra for the lowest-energy WSe₂-A exciton resonance in region 2 of device D1 when the local top-gate voltage V_{top} is tuned from 0.5 V to -3.5 V. Region 2 is not affected when the hole concentration is tuned in region 1 by V_{top} . **b**, Reflection

contrast spectra for the WSe₂-A exciton in region 2 when the global back gate is tuned from -0.95 V to -1.05 V. The inset shows a zoomed-in view of the exciton peak. The spectral change is monotonic and approximately linear with carrier concentration.

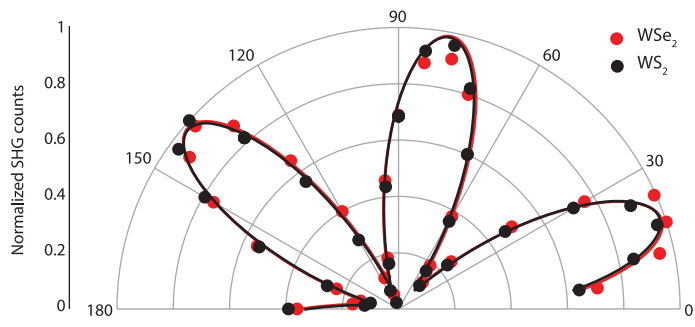


Extended Data Fig. 2 | ODRC signal measured at very low frequencies for a range of modulation voltages. V_{mod} , modulation voltage.



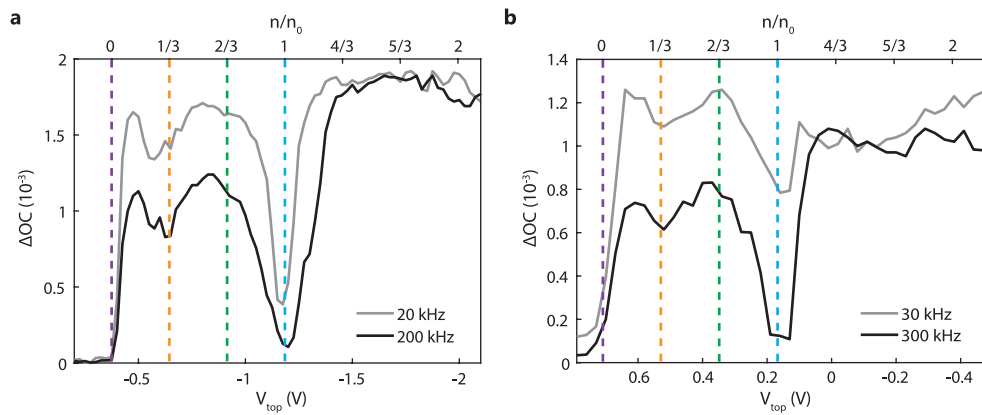
Extended Data Fig. 3 | Calibration of hBN dielectric constant. **a**, MoSe₂ A exciton peak intensity measured while tuning the voltages of the top graphite gate and back Si gate. **b**, The extracted charge-neutral points (CNP, dots) for

each Si back gate, corresponding to the top graphite gate voltages that bring the system to zero net charge. The black line is a linear fit to the data, from which the relative gate efficiency is determined.



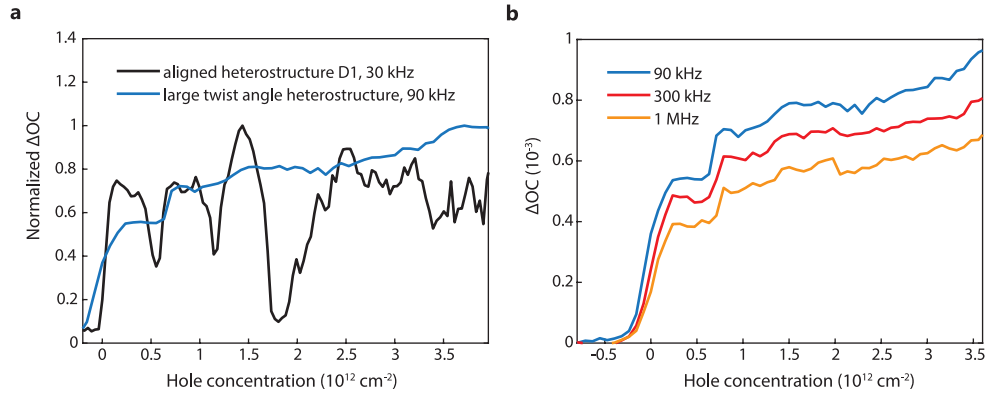
Extended Data Fig. 4 | Determination of WSe_2 and WS_2 flake alignment.

Polarization-dependent SHG signal on monolayer WSe_2 (red circles) and WS_2 (black circles) regions of device D1 and corresponding fittings (red and black curves, respectively).



Extended Data Fig. 5 | ODRC signal for other aligned WSe₂/WS₂ heterostructures. **a, b,** ODRC signal at low (grey) and high (black) frequency from charge-neutral to moderate hole doping in devices D2 (**a**) and D3 (**b**). The

dashed lines are guides to the eye at hole concentrations of $n = 0$ (purple), $n = n_0/3$ (orange), $n = 2n_0/3$ (green) and $n = n_0$ (blue).



Extended Data Fig. 6 | ODRC signal for a large-twist-angle WSe₂/WS₂ heterostructure. **a**, Normalized ΔOC for a large-twist-angle heterostructure (D4, blue) and an aligned heterostructure (D1, black). The misaligned

heterostructure does not show any insulating features. **b**, The frequency dependence of the large-twist-angle heterostructure signal shows a characteristic RC circuit fall-off with increasing frequency.